



Graphene oxide as structure-directing and morphology-controlling agent for the syntheses of heterostructured graphene-Bi₂MoO₆/Bi_{3.64}Mo_{0.36}O_{6.55} composites with high photocatalytic activity

Jian-Ping Zou^a, Jun Ma^a, Qiong Huang^a, Sheng-Lian Luo^{a,*}, Jian Yu^a, Xu-Biao Luo^a, Wei-Li Dai^a, Jing Sun^b, Guo-Cong Guo^b, Chak-Tong Au^{a,c}, Steven L. Suib^{d,*}

^a Key Laboratory of Jiangxi Province for Persistent Pollutants Control and Resources Recycle, Nanchang Hangkong University, Nanchang, Jiangxi 330063, P.R. China

^b State Key Laboratory of Structural Chemistry, Fujian Institute of Research on the Structure of Matter, Chinese Academy of Sciences, Fuzhou, Fujian 350002, P.R. China

^c Department of Chemistry, Hong Kong Baptist University, Kowloon Tong, Hong Kong, P.R. China

^d Department of Chemistry, University of Connecticut, Storrs, CT, USA

ARTICLE INFO

Article history:

Received 8 January 2014

Received in revised form 7 March 2014

Accepted 19 March 2014

Available online 27 March 2014

Keywords:

Bismuth molybdate
Controllable synthesis
Graphene
Graphene oxide
Photocatalyst

ABSTRACT

We report the new roles of graphene oxide (GO) as structure-directing and morphology-controlling agents in the nucleation and growth of heterostructured Bi₂MoO₆/Bi_{3.64}Mo_{0.36}O_{6.55} composites. The heterostructured composites have been fabricated through a facile one-step hydrothermal method, among which the interfacial contact between Bi₂MoO₆/Bi_{3.64}Mo_{0.36}O_{6.55} and graphene is achieved. The as-prepared composites were characterized by powder X-ray diffraction, UV–vis diffuse reflectance spectroscopy, scanning electron microscopy, transmission electron microscopy, and Raman spectroscopy. The composition, morphology and structure of the composites can be controlled by regulating the amount of GO used in the synthesis. We proposed a plausible mechanism for their formation, and evaluated them for the photocatalytic degradation of Rhodamine B (RhB). Among them, the 1% graphene-Bi₂MoO₆/Bi_{3.64}Mo_{0.36}O_{6.55} (1%G-BMO) composite performs the best. The efficacy of 1%G-BMO is attributed to the optimal Bi₂MoO₆/Bi_{3.64}Mo_{0.36}O_{6.55} phase ratio, the unique morphology and structure, as well as the effective separation of photogenerated electrons and holes.

© 2014 Elsevier B.V. All rights reserved.

1. Introduction

In the past decade, inorganic materials with controlled morphology, structure and composition were constructed and studied for fundamental researches and potential technological applications [1]. The properties of these functional materials can be easily tuned through the variation of building units during construction [2]. Until now, a wide variety of materials with special structures, including metals [3], nonmetals [4], semiconductors [5] and copolymers [6] were successfully prepared based on different formation mechanisms. The common strategies are to use surfactants

(e.g. CTAB, SDBS, and SDS) [7], polymers (e.g. PVP and PEO) [8], ionic liquids [9] and chelating agents (e.g. EDTA, citric acid, and sodium tartrate) [10] to direct the self-assembly of materials for the formation of a particular structure.

Graphene is a kind of two-dimensional (2D) carbon material. Graphene displays great mechanical strength, huge specific surface area, excellent adsorptivity as well as remarkable electronic and thermal conductivity [11]. With such properties graphene can be employed for various applications. For example, graphene is used as a template to control the microstructure of mesoporous silica [12], and is employed as an atomic template and structural scaffold for the synthesis of graphene-organic hybrid solar cells [13]. Furthermore, graphene modified by surfactants is also used for self-assembly with metal oxide for electrochemical energy storage [14].

As another specific branch of carbon materials, graphene oxide is a derivative of graphene and its role is usually as an

* Corresponding authors. Tel.: +86 791 83863688/+1 860 4862797;

fax: +86 791 83953373/+1 860 4862981.

E-mail addresses: sllou@hnu.edu.cn (S.-L. Luo), steven.suib@uconn.edu (S.L. Suib).

important intermediate to obtain graphene via chemical reduction, thermally mediated reduction or electrochemical reduction and chemically modified graphene through established colloidal suspension methodologies [15]. In redox reactions using noble metal/GO nanocomposites as catalyst, GO not only acts as a support for reduced nanoparticles but also as a conductive material for electron transfer [16]. In addition, GO is used in the fields of electrochemical sensors and electroanalytical chemistry [17]. However, in the literature GO is rarely used as agent for controllable synthesis of materials. In fact, with a large number of hydrophilic oxygen-containing groups on a hydrophobic basal plane, GO behaves as an amphiphilic macromolecule. With such structural features, GO can be utilized as a special kind of surfactant [18]. In addition, the properties of GO mainly vary due to different stoichiometric compositions (C_xO_y) depending upon its degree of oxidation [19]. Therefore, it is envisaged that in the synthesis of nanostructured materials, one can control the composition, structure and morphology of materials through the use of heavily oxidized GO as a surfactant.

Bismuth molybdate is a dielectric and shows catalytic behavior and luminescence properties [20]. This material functions as an excellent photocatalyst for water splitting as well as for the degradation of organic pollutions [21]. Up to now, there are studies on the effect of crystallinity, size, and morphology on photocatalytic activity [22], but attempts to relate performance with composition, morphology and structure are rare. Recently, we reported the synthesis of ternary heterostructured photocatalysts TiO_2 - $Bi_2MoO_6/Bi_{3.64}Mo_{0.36}O_{6.55}$ [23]. Through the adjustment of pH, ethanol amount and TiO_2 loading, we successfully controlled the composition, structure and morphology of the catalysts.

To conduct further studies of the controllable synthesis and enhanced photocatalytic activities of bismuth molybdate, we investigate the use of other templates as controlling agents. With the idea that GO can be utilized as an agent to control the composition, structure and morphology of bismuth molybdate, we studied possible roles in the controllable synthesis of graphene- $Bi_2MoO_6/Bi_{3.64}Mo_{0.36}O_{6.55}$, and the resultant composites are denoted hereinafter as G-BMO. Based on these results, we propose a plausible formation mechanism of the materials and then evaluate the photocatalytic activity of G-BMO using the degradation of Rhodamine B (RhB) as a model reaction. The goals of the investigations are (i) to gain insights into the controlled synthesis of photocatalysts with excellent performance, and (ii) to explore the roles of GO for the design and fabrication of novel graphene-based heterostructured composites for technological applications.

2. Experimental

2.1. Materials and measurements

All reagents were analytical grade and used as received without further purification. The X-ray diffraction (XRD) patterns of the samples were collected over a Bruker D8 ADVANCE using monochromatized Cu K α ($\lambda = 1.5406 \text{ \AA}$) radiation. The XRD data for indexing and cell-parameter calculations were collected in the $10\text{--}60^\circ$ (2θ) range (scan speed: 2° min^{-1}). The morphology of samples was studied using a scanning electron microscope (SEM, FEI, Holland) and a transmission electron microscope (TEM). Raman spectra were recorded on a microscopic confocal Raman spectrometer (JY LabRam HR800) with a laser source of 785 nm for excitation. X-ray photoelectron spectroscopy (XPS) measurements were done with a VG Escalab 250 spectrometer equipped with an Al anode (Al K $\alpha = 1486.7 \text{ eV}$). Fourier transform infrared (FTIR) spectra were recorded on a Bruker VERTEX 70 spectrometer using the KBr pellet

technique. UV–vis diffuse reflectance spectra were collected with a Hitachi U-3900H UV–vis spectrophotometer at room temperature (RT). Thermogravimetry and differential thermal analyses (TG-DTA) were performed on a PerkinElmer Diamond thermoanalyzer under air in the range of $0\text{--}600^\circ\text{C}$ at a heating rate of 10°C/min .

Electrochemical measurements were performed on a CHI660D electrochemical workstation (Shanghai Chenhua, China) using a standard three-electrode cell with a working electrode, a counter electrode (Pt wire), and a standard reference calomel electrode in saturated KCl. The working electrode was prepared by dip-coating: Briefly, 200 mg of photocatalyst was suspended in 200 μL ethanol in the form of a slurry and was dip-coated onto a $1 \text{ cm} \times 1 \text{ cm}$ fluorine-tin oxide (FTO) glass electrode with a sheet resistance of 15Ω . Then the film was dried under ambient conditions, and coated with two drops of 0.05% naphthol ethanol solution before being dried at 100°C for 3 h. The electrochemical impedance spectroscopic (EIS) investigation was carried out at open circuit potential in the presence of a 2.5 mM $K_3[Fe(SCN)_6]/K_4[Fe(SCN)_6]$ (1:1) mixture (as a redox probe) in 0.5 M K_2SO_4 aqueous solution. The flat band potentials (V_{fb}) were electrochemically determined from the Mott–Schottky plots [24]. Prior to and during all measurements, the electrolyte (0.5 M K_2SO_4) was purged with nitrogen.

2.2. GO and G-MBO syntheses

2.2.1. Synthesis of GO

In order to enhance the hydrophilic and high oxidation degree of GO and also be easier to obtain monolayer GO by mechanical exfoliation, an improved method was used to prepare graphite oxide [25]. Briefly, a solution of concentrated H_2SO_4/H_3PO_4 (9:1, volume ratio) was added to a mixture of graphite flakes (325 mesh) and $KMnO_4$ (1:6, weight ratio), and the mixture was heated to 50°C and magnetically stirred for 12 h. After being cooled down to RT, the mixture was poured into an icy solution of 30% H_2O_2 . The solid was filtered out and subject to cycles of washing with deionized water, and then vacuum-dried at RT overnight. Finally, the generated graphite oxide was dispersed in water (1 mg mL^{-1}) and subject to sonication for 1 h to form an aqueous dispersion of exfoliated GO.

2.2.2. Synthesis of heterostructured G-BMO composites

The synthesis of G-BMO composites using different amounts of GO oxide (weight ratios of GO to $Bi_2MoO_6/Bi_{3.64}Mo_{0.36}O_{6.55}$ are 0.5, 1.0, 3.0, 7.5, and 10.0 wt%) is as follows. First, $Bi(NO_3)_3 \cdot 5H_2O$ (2.5 mmol) was dissolved in 10 mL deionized water under magnetic stirring for 30 min. A solution of stoichiometric amount of $(NH_4)_6Mo_7O_{24} \cdot 4H_2O$ (0.18 mmol) dissolved in 5 mL deionized water was slowly added to the $Bi(NO_3)_3$ solution under stirring for 15 min. Then stoichiometric amount of the as-prepared GO dispersion was slowly added into the above mixed solution and magnetically stirred for 1 h. After that, 2.5 mL ethanol and stoichiometric amount of hydrazine hydrate (10 μL hydrazine hydrate to 1 mg GO) were added to the above mixed solution, followed by dilution (to 80 mL) with deionized water. After stirring for uniform dispersion, the resultant mixture was adjusted to a pH of 8.5 using a solution of concentrated ammonia, and then transferred to a 100 mL Teflon-sealed autoclave for hydrothermal treatment at 150°C for 5 h. With the autoclave and its content cooled to RT, the product was recovered by filtration, washed by water and ethanol, and fully dried at 60°C in an oven to obtain the G-BMO composites. Hereinafter, the $Bi_2MoO_6/Bi_{3.64}Mo_{0.36}O_{6.55}$ loaded with 0.5%, 1.0%, 3.0%, 7.5%, and 10.0% GO synthesized at pH 8.5 are denoted as 0.5%G-BMO, 1.0%G-BMO, 3.0%G-BMO, 7.5%G-BMO, 10.0%G-BMO, and 20.0%G-BMO, respectively. For comparison, the $Bi_2MoO_6/Bi_{3.64}Mo_{0.36}O_{6.55}$ (BMO) composite was prepared at pH

8.5 following the same procedures but without any involvement of GO. We also obtained a sample of graphene (GR) through the same procedures but without the participation of $\text{Bi}(\text{NO}_3)_3 \cdot 5\text{H}_2\text{O}$ and $(\text{NH}_4)_6\text{Mo}_7\text{O}_{24} \cdot 4\text{H}_2\text{O}$.

2.3. Photocatalytic reactions

Photocatalytic activities of samples were evaluated using the degradation of rhodamine B (RhB) under visible light as model reaction. A 300 W Xe lamp (PerfectLight, wavelength range: $320 \text{ nm} \leq \lambda \leq 780 \text{ nm}$, light intensity: 160 mW/cm^2) was used as the light source with a 420 nm cutoff filter to provide visible-light irradiation. For the degradation of RhB, 0.05 g of photocatalyst was added into 100 mL of RhB solution (10^{-5} M) under the irradiation of visible light. Before illumination, the solution was stirred for 1 h in the dark to reach adsorption–desorption equilibrium between the photocatalyst and RhB. At 10 min intervals, the solution was sampled (5 mL) and the concentration of RhB was detected by recording the absorbance at the characteristic band of 553 nm using a Hitachi U-3900H UV–visible spectrophotometer.

3. Results and discussion

3.1. Materials characterization

3.1.1. XRD

All relevant XRD peaks were identified and indexed based on the available JCPDS (Joint Committee for Powder Diffraction Studies) data. Across the catalysts there is no detection of any peaks attributable to impurities. As shown in Figure S1, the diffraction peak at around $2\theta = 9.0^\circ$ corresponds to the (0 0 1) reflections of GO. Due to the large amount of oxygen-containing functional groups on the graphite sheets, the interlayer spacing (0.97 nm) is larger than that of the GO obtained by other synthetic methods. Similar results were reported by Marcano et al. [25].

Fig. 1 shows the XRD patterns of BMO, Bi_2MoO_6 , $\text{Bi}_{3.64}\text{Mo}_{0.36}\text{O}_{6.55}$, 0.5%G-BMO, 1.0%G-BMO, 3.0%G-BMO, 7.5%G-BMO, and 10.0%G-BMO. There are mixed phases of orthorhombic Bi_2MoO_6 (JCPDS No. 00-021-0102) and cubic $\text{Bi}_{3.64}\text{Mo}_{0.36}\text{O}_{6.55}$ (JCPDS No. 00-043-0446) in the G-BMO composites. No signals are ascribed to graphene species, even up to a GO level of 10%, which might be due to the low amount and relatively low diffraction intensity of graphene in the composites and the efficient exfoliation of graphene by BMO [26]. With the increase of GO addition, the characteristic (1 1 1) peak of $\text{Bi}_{3.64}\text{Mo}_{0.36}\text{O}_{6.55}$ appears and increases in intensity, while the characteristic (1 3 1) and (0 2 0) peaks of Bi_2MoO_6 notably diminish (Fig. 1). The phenomenon shows that as a result of GO introduction, the formation of $\text{Bi}_{3.64}\text{Mo}_{0.36}\text{O}_{6.55}$ becomes more favorable than that of Bi_2MoO_6 . When the GO amount increases to 20 wt%, the XRD pattern of the 20.0%G-BMO composite is very similar to that of 10.0%G-BMO, which means that the phase transition will occur only within a certain limit of GO content. In order to determine the definite content of Bi_2MoO_6 and $\text{Bi}_{3.64}\text{Mo}_{0.36}\text{O}_{6.55}$ among the as-prepared catalysts, the phase content fitting and peak deconvolution of the XRD patterns were done with a least-square method applying the GSAS program to calculate the mole ratio of Bi_2MoO_6 and $\text{Bi}_{3.64}\text{Mo}_{0.36}\text{O}_{6.55}$ [27]. As shown in Figure S2 and Table S1, the molar ratio of $\text{Bi}_{3.64}\text{Mo}_{0.36}\text{O}_{6.55}$ to Bi_2MoO_6 become larger with the increase of GO loading amount (the molar amount of $\text{Bi}_{3.64}\text{Mo}_{0.36}\text{O}_{6.55}$ is 0.86% and 44.27% in BMO and 10.0%G-BMO, respectively), which indicates a new role of GO as a structure-directing agent. Therefore, it is hence possible to fabricate G-BMO composites that are different in phase composition by regulating the extent of GO addition.

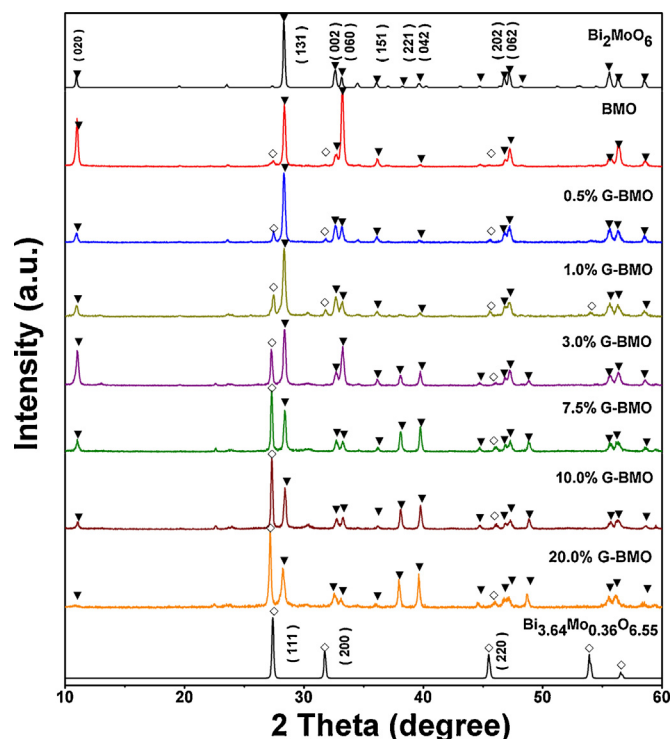


Fig. 1. XRD patterns of Bi_2MoO_6 , $\text{Bi}_{3.64}\text{Mo}_{0.36}\text{O}_{6.55}$, BMO and G-BMO.

3.1.2. SEM and TEM

The morphology of the as-prepared BMO and G-BMO composites was examined by SEM and TEM. The low- and high-magnification SEM images are shown in Figs. 2(a–d) and S3, respectively. Over the BMO sample, one can see two kinds of morphology, one is strip-like nanosheets having length of 6–8 μm , suggesting favorable crystal growth of Bi_2MoO_6 along the normal of (0 2 0) and (0 6 0) facets; and the other is fish-scale nanoflakes with average diameters of 250–300 nm corresponding to the $\text{Bi}_{3.64}\text{Mo}_{0.36}\text{O}_{6.55}$ phase (Figs. 2a and S3a) [23,28]. At 1 wt% GO, there is decrease of strip-like nanosheets as well as the detection of irregular-polygon nanosheets with size of about 1–1.5 μm (Figs. 2b and S3b). At 3 wt% GO, there is the detection of graphene and nanoflakes 300–500 nm in size, the latter suggests a stronger growth along the normal of the (1 1 1) $\text{Bi}_{3.64}\text{Mo}_{0.36}\text{O}_{6.55}$ crystal facet. At 10 wt% GO, the nanosheets stack into a blocky structure wrapped by graphene. As shown in Fig. 2(e–h), the TME image of the as-prepared samples with better ultrasonic dispersion show better uniformity than that of SEM and the change of morphology growth are both clearly observed. A combined analysis of the XRD (Fig. 1), SEM and TEM results suggests continuous growth of $\text{Bi}_{3.64}\text{Mo}_{0.36}\text{O}_{6.55}$ crystals along the crystal face of the (1 1 1) facet as well as continuous growth of Bi_2MoO_6 along the crystal faces of the (2 2 1) and (0 4 2) facets (Fig. 2). In other words, with the addition of GO, there is a change in terms of the structure, composition and morphology of the G-BMO composites.

3.1.3. FTIR

Fig. 3a shows the FTIR spectra of GO, BMO and 1%G-BMO. FTIR spectra of GO show the characteristic peaks including O–H stretching at 3396 cm^{-1} , C=O stretching at 1727 cm^{-1} , skeletal vibration of unoxidized graphitic domains at 1620 cm^{-1} , O–H deformation at 1406 cm^{-1} , C–OH stretching at 1223 cm^{-1} , and C–O stretching at 1050 cm^{-1} , confirming the successful and efficient oxidation of graphite [25]. Compared with the GO spectrum, the spectrum of 1%G-BMO shows significant decline of intensity with the bands that

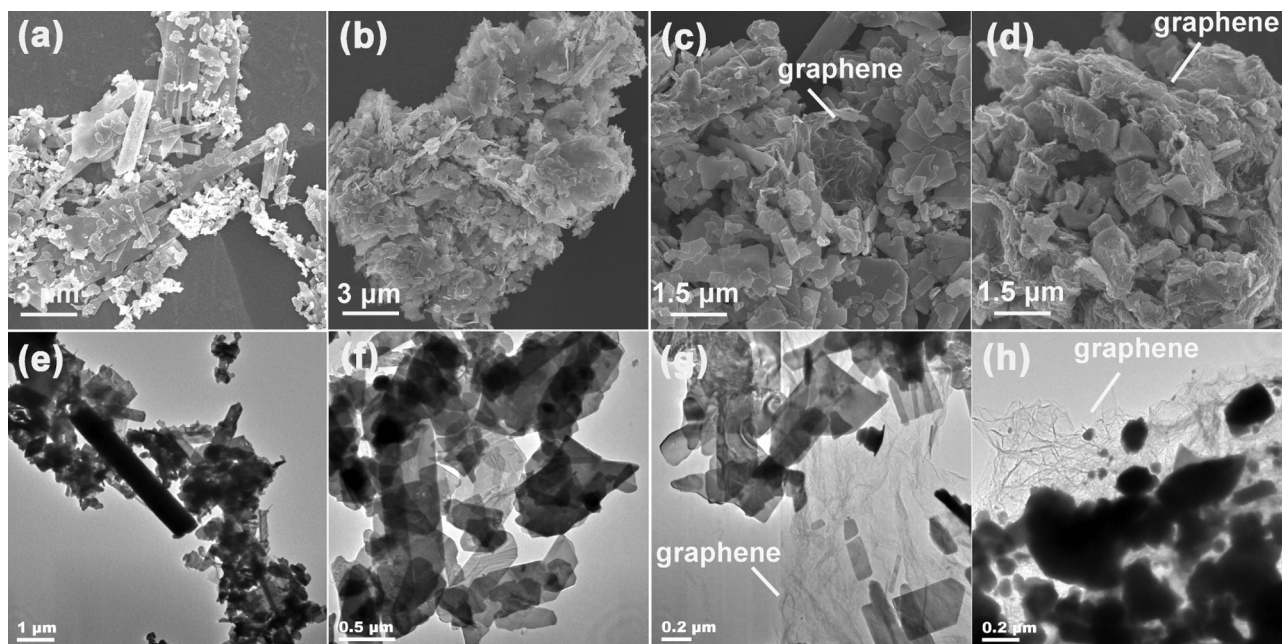


Fig. 2. SEM (a–d) and TEM (e–h) images of BMO, 1.0%G-BMO, 3.0%G-BMO and 10%G-BMO.

are associated with the oxygen functional groups (i.e. O–H, C=O, C–OH, and C–O), suggesting that the GO in the 1%G-BMO composite is reduced. The strong bands in the range of 400–1000 cm^{-1} of BMO and 1%G-BMO shown in Fig. 3a are attributed to the vibrations of BMO chemical bonds [22], while the one around 1462 cm^{-1} may be a characteristic peak of 1%G-BMO. The peaks in the 1250–1750 cm^{-1} range detected over 1%G-BMO are stronger than those detected over BMO, confirming the formation of strong bonding between graphene sheets and BMO in the G-BMO composites.

3.1.4. Raman

Shown in Fig. 3b are the results of Raman spectroscopic investigation. Two bands are observed in the 1200–1800 cm^{-1} range for GO and 1%G-BMO. They are the G and D bands of carbonaceous materials [29]. The former is usually assigned to in-plane stretching of ordered sp^2 bonded carbon, whereas the latter is ascribed to defects such as edges and vacancies and/or disordered carbon. A typical G band at 1599 cm^{-1} and a prominent D band at 1328 cm^{-1} with a D/G intensity ratio of 1.02 are observed over GO. In the case of 1%G-BMO, the G band is at 1590 cm^{-1} and the D band at 1314 cm^{-1} , and the D/G intensity ratio is 1.39. This phenomenon collides with the usual case that the D/G intensity ratio will decrease when GO is reduced. But it is deduced that there is GO reduction to graphene species during the synthesis of 1%G-BMO, and the aggregation of GR is inhibited by the existence of BMO [30–32]. In addition, after hydrothermal reduction with hydrazine, the D and G peaks are both red-shift because the oxygen functional groups in GO sheets have been removed and the conjugated graphene network (sp^2 carbon) have been re-established. As for the Raman signals of the G-BMO composites, the peaks in the range of 700–850 cm^{-1} can be ascribed to the stretching modes of Mo–O bonds [33]. The peaks between 700 and 900 cm^{-1} detected over 1%G-BMO are slightly different from those detected over BMO, both in shape and position, plausibly a consequence of Bi–C or Mo–C bonding. The results indicate significant interaction between GR and $\text{Bi}_2\text{MoO}_6/\text{Bi}_{3.64}\text{Mo}_{0.36}\text{O}_{6.55}$ consistent with the results of FTIR investigation.

3.1.5. XPS

The reduction of GO to GR during the hydrothermal process can also be evidenced by the XPS results. The C 1s spectra of GO and 1%G-BMO are displayed in Fig. 4. For GO, the C 1s profile can be deconvoluted into three peaks that correspond to sp^2 carbon (C=C, 284.6 eV), epoxy/hydroxyls (C–O, 286.9 eV) and carboxylates (O–C=O, 288.4 eV) [33]. We determined the relative level of oxidation based on the percentage of oxidized and graphitic carbon. The approach is more reliable than the method based on the C/O ratio because it is difficult to fully dehydrate a GO sample [34]. The GO generated in this study shows “oxidized carbon to graphitic carbon” ratio of 69:31, comparable to those of graphite oxide synthesized from graphite using similar oxidation treatment [25]. For the heterostructured 1%G-BMO composite, the marked loss of oxygen-containing functional groups is observed, which indicates the sufficient reduction of GO to graphene after coupling $\text{Bi}_2\text{MoO}_6/\text{Bi}_{3.64}\text{Mo}_{0.36}\text{O}_{6.55}$ with GO via the hydrothermal method [35].

3.1.6. UV–vis

The optical properties of the as-prepared G-BMO composites were investigated. As shown in Fig. 5, all the as-prepared samples exhibit strong absorption in the visible region and the absorption edges are around 450–550 nm. With the increase of graphene content, there is red shift of the absorbance edge and enhancement of absorption intensity, in accordance with the change of sample color (Figure S4). The result indicates that the GO in G-BMO composites is well deoxygenated and is reduced to GR.

3.1.7. Thermogravimetric analysis (TGA)

The TGA curves for the BMO and 1.0%G-BMO composites (Figure S5) show that the mass loss in the range of 0–600 $^{\circ}\text{C}$ with a heating rate of 10 $^{\circ}\text{C}/\text{min}$. Before 300 $^{\circ}\text{C}$, the mass loss can be attributed to the removal of absorbed water and the decomposition of residual oxygen functional groups of graphene [36]. At the final temperature of 600 $^{\circ}\text{C}$, the weight of BMO and 1.0%G-BMO become unchanged and the TG% D-value is about 1.18%, which is due to the oxidation

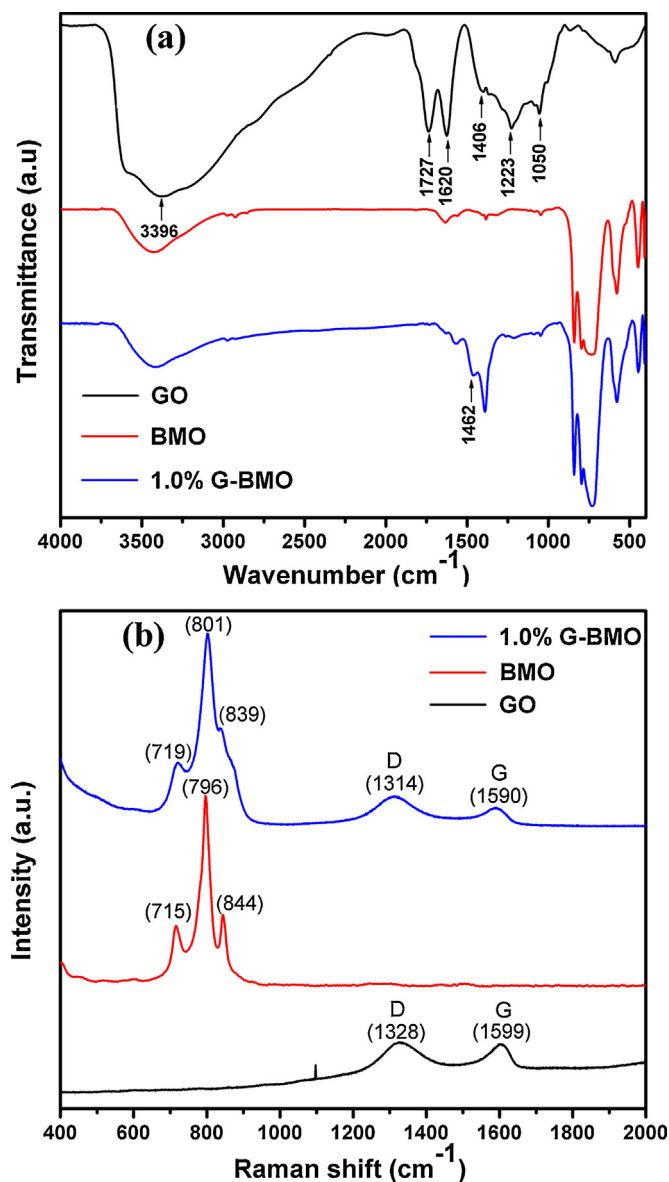


Fig. 3. (a) FTIR spectra and (b) Raman spectra of GO, BMO and 1.0%G-BMO.

of carbon. This result reveals that the real graphene content (1.18%) in the composite is close to the additive amount.

3.2. Formation mechanism of G-BMO composites

According to the results of XRD and SEM analyses, one can control the composition, structure and morphology of bismuth molybdate by regulating the amount of GO in the reaction system. During the formation of bismuth molybdate in the presence of ethanol, Bi^{3+} (or MoO_4^{2-}) reacts with ethanol to form a M-ethanol ($\text{M} = \text{Bi}^{3+}$ or MoO_4^{2-}) complex through hydrogen bonding between Bi^{3+} (or MoO_4^{2-}) and ethanol [23,33], and at pH equal to 8.5, there is the generation of the mixed phase of Bi_2MoO_6 and $\text{Bi}_{3.64}\text{Mo}_{0.36}\text{O}_{6.55}$ [23,33]. Similar to those reports, in our case of adding GO, M-ethanol ($\text{M} = \text{Bi}^{3+}$ or MoO_4^{2-}) complexes are also formed via chemical and hydrogen bonds generated from inter-linkage of the water molecules and oxygen-containing groups on GO layers, such as hydroxyl, carboxylic acid and ether epoxy functionalities decorating the basal planes and edges of GO. With increase of GO addition, there are more active sites (oxygen-containing groups) on the GO layers available for the capture of

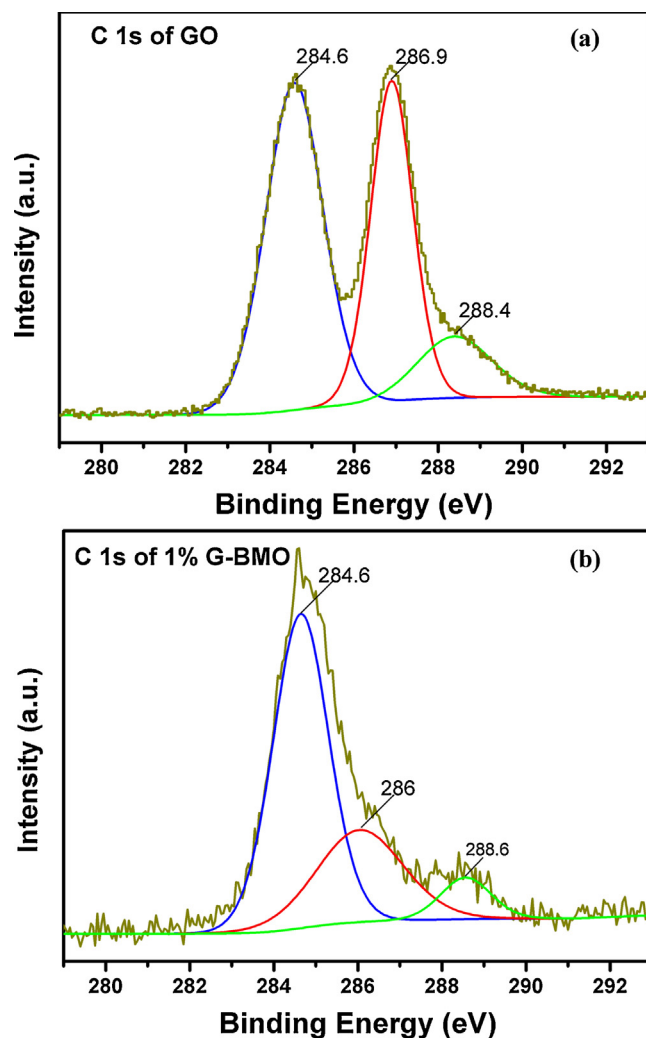


Fig. 4. C 1s spectra of (a) GO and (b) 1.0%G-BMO.

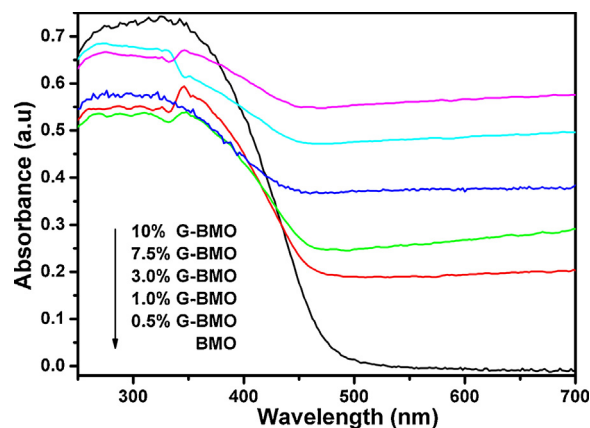


Fig. 5. UV-vis diffuse reflectance spectra of BMO and G-BMO composites.

Bi^{3+} or Bi-ethanol complexes through electrostatic force and hydrogen bonding. In other words, with increase of GO in the reaction system, there is less Bi^{3+} or Bi-ethanol complexes available for interaction with MoO_4^{2-} ions. The result is the favorable formation of $\text{Bi}_{3.64}\text{Mo}_{0.36}\text{O}_{6.55}$ phase during the hydrothermal process, and the morphology of G-GMO changes from nanosheets to blocks

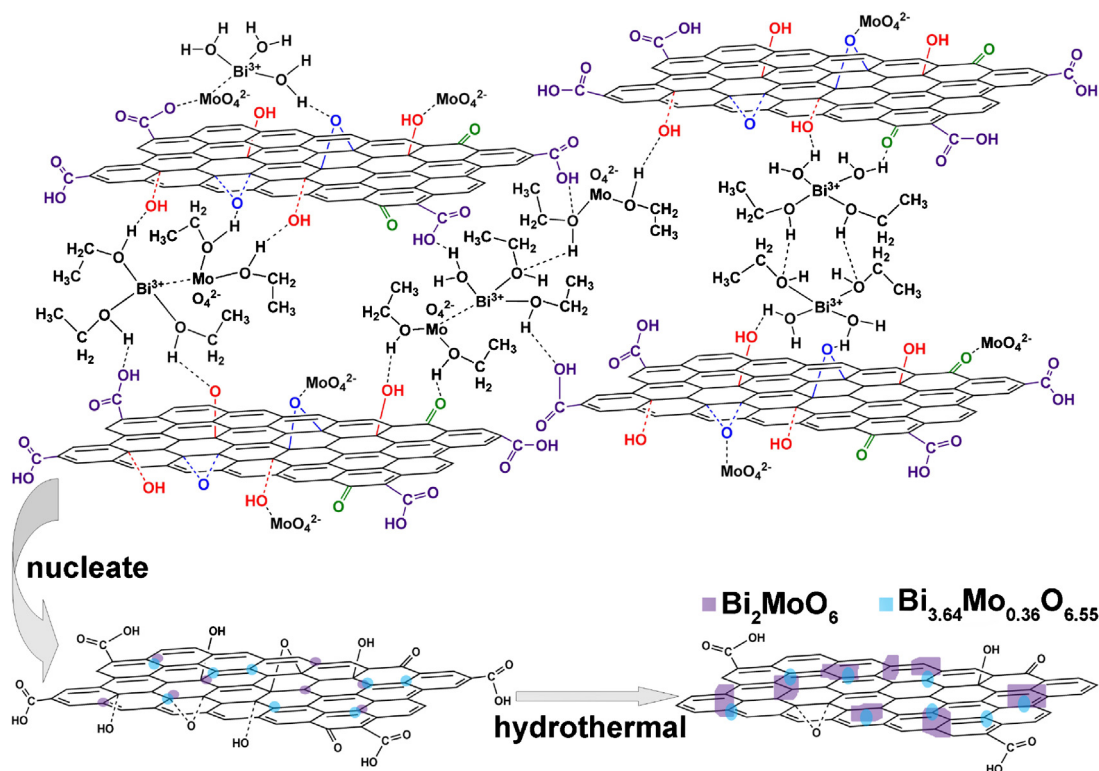


Fig. 6. Schematic illustration of the mechanism for G-BMO formation.

as illustrated above based on the results of XRD, SEM and TEM investigation. Simultaneously, the GO layers are deoxygenated and reduced to GR that is closely bonded with BMO. According to such understandings, a growth mechanism is illustrated in Fig. 6 to explain the controllable synthesis of G-BMO composites through the tuning of GO addition.

3.3. Photocatalytic activity

Rhodamine B (RhB) was selected as model pollutant to evaluate the photocatalytic activity of the as-prepared catalysts under visible light irradiation ($\lambda > 420$ nm). Fig. 7a shows the adsorption step for 60 min to establish the adsorption/desorption equilibrium and the photodegradation of RhB for 60 min of BMO with different amounts of GO (C is RhB absorption at a wavelength of 553 nm and C₀ is absorption at initial concentration of RhB before adsorption equilibrium on catalysts). Furthermore, when BMO is added with GO, the adsorption amount of RhB is enhanced markedly due to the increasing content of graphene with high specific surface area. In the photocatalytic process, the 1.0%G-BMO performs the best as compared with other as-prepared samples. (The removal rate of 100% and the temporal evolution of the spectra are shown in Figure S6.) For the samples with higher ratio of GO, adsorption is the dominant effect on the final content of RhB and the photocatalytic activity is very poor. From the XRD (Fig. 1), SEM and TEM (Figs. 2 and S3) results, the 1%G-BMO composite is a result of optimization through the tuning of composition, morphology and structure. Another reason for its excellent performance is that the GR in G-BMO composites can effectively restrain the recombination of photogenerated charge carriers.

As shown in Fig. 7b, the degradation/removals of RhB over 1.0%G-BMO in the dark, in a blank run (without a catalyst) or that over GR under visible light irradiation are low. Also a physical

mixture of BMO (99 wt%) and GR (1 wt%) shows performance similar to that of BMO which is worse than that of 1%G-BMO. The excellent performance of 1%G-BMO is due to the formation of bonds between BMO and graphene.

We determined the major active species accounting for the degradation of RhB over 1%G-BMO using •OH (1 mM isopropanol), h⁺ (1 mM sodium oxalate) and •O₂⁻ (1 mM benzoquinone) scavengers. As shown in Fig. 8a, the photocatalytic degradation of RhB is just slightly affected by the addition of isopropanol, while the addition of sodium oxalate and benzoquinone obviously suppress the degradation of RhB. The results clearly indicate that h⁺ and •O₂⁻ rather than •OH are the major active species. When O₂ is bubbled to enrich the oxygen in the solution, there is a slight increase of RhB degradation. This phenomenon reveals that the reaction of molecular oxygen with photogenerated electrons for the generation of •O₂⁻ is important for RhB degradation over G-BMO. In consideration of photosensitization of RhB, the investigation of the photodegradation of 2,4-dichlorophenol (a colorless organic pollutant, 286 nm as the detection wavelength) was carried out. As shown in Figure S9, the results are very similar to that of the degradation of RhB. Therefore, the influence of photosensitization has been ruled out.

We checked the stability and efficiency of 1.0%G-BMO in four repetitive runs of photocatalytic degradation of RhB under visible light (Fig. 8b), and found that the change in photocatalytic performance across the four runs is minimal. The result indicates that the 1.0%G-BMO composite is highly stable and is suitable for practical use.

3.4. Mechanism of photocatalytic activity enhancement

With 2D π -conjugation structure, GR acts as an electron acceptor and a transporter [37]. In Fig. 9, the typical electrochemical

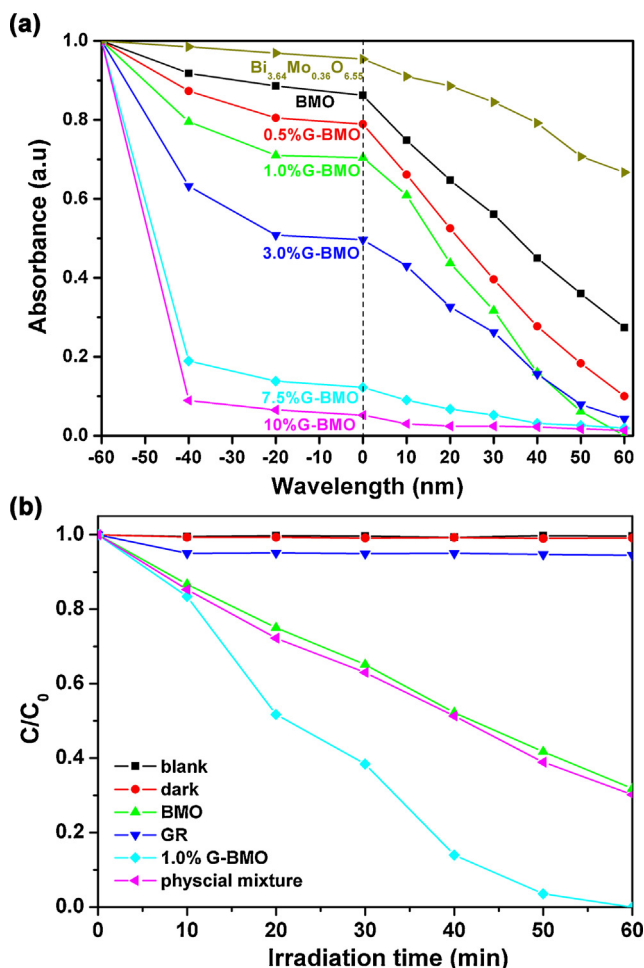


Fig. 7. (a) Photodegradation of RhB in 60 min over BMO and G-BMO composites and (b) comparison of RhB degradation over different samples under visible light (absorbance at a particular time and that at initial concentration of RhB before adsorption equilibrium on catalysts are denoted as C and C_0 , respectively.)

impedance spectra (EIS) of BMO and 1.0%G-BMO are presented as Nyquist plots, with the former showing a semicircle bigger than that of the latter. Based on the results, 1.0%G-BMO is more efficient than BMO in terms of interfacial charge transfer as well as separation of photogenerated electrons and holes. A similar phenomenon was observed by Zhang et al. [38].

Furthermore, the electrochemical properties of the photocatalysts were studied using a standard three-electrode cell. Figure S7 shows the Mott–Schottky plots with Bi_2MoO_6 and $\text{Bi}_{3.64}\text{Mo}_{0.36}\text{O}_{6.55}$ being working electrode (0.5 M K_2SO_4 as electrolyte). Reversed sigmoidal plots are observed with an overall shape consistent with that typical for n-type semiconductors. The V_{fb} as calculated from the x intercepts of the linear region are found to be -0.54 and -0.38 V vs. $\text{Hg}/\text{Hg}_2\text{Cl}_2$ (equivalent to -0.30 and -0.14 V vs. NHE), respectively, for Bi_2MoO_6 and $\text{Bi}_{3.64}\text{Mo}_{0.36}\text{O}_{6.55}$, not far away from the V_{fb} value (-0.32 V vs. NHE) of Bi_2MoO_6 calculated by Long et al. [39]. As an inherent property of semiconductors, V_{fb} equals the Fermi Level (E_F) of an n-type semiconductor. Therefore, the Fermi levels (E_F) of Bi_2MoO_6 and $\text{Bi}_{3.64}\text{Mo}_{0.36}\text{O}_{6.55}$ are -0.30 and -0.14 V vs. NHE, respectively; and the calculated work function of GR is -4.42 eV vs. vacuum (-0.08 V vs. NHE) [40], which is more negative than the Fermi level of Bi_2MoO_6 and $\text{Bi}_{3.64}\text{Mo}_{0.36}\text{O}_{6.55}$.

The bottom of the conduction band (CB) of n-type semiconductors is more negative (about 0–0.2 V) than the flat band potential, which is dependent on the electron effective mass and carrier concentration [33,41]. In consideration of this, the E_{CB}

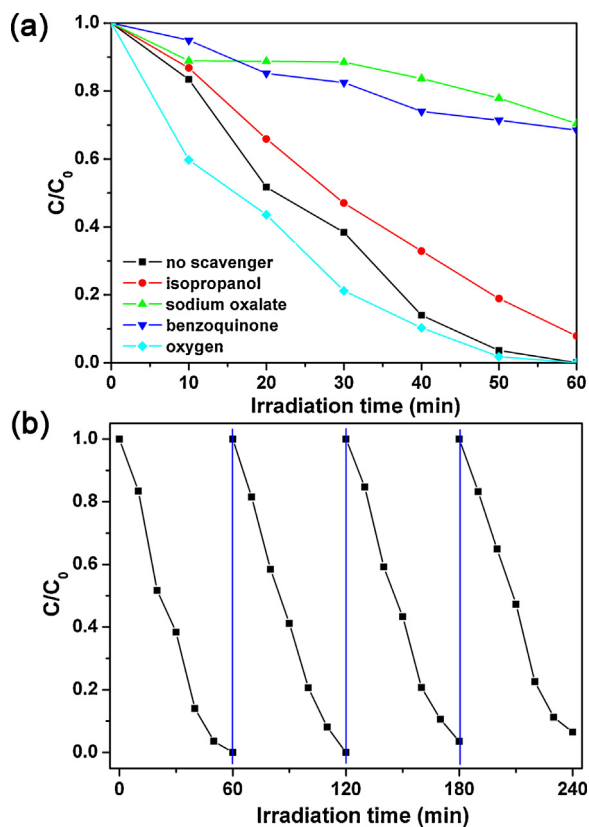


Fig. 8. (a) Effects of scavengers and oxygen on photodegradation of RhB over 1.0%G-BMO and (b) repetitive runs of the photodegradation of RhB over 1.0%G-BMO under visible light.

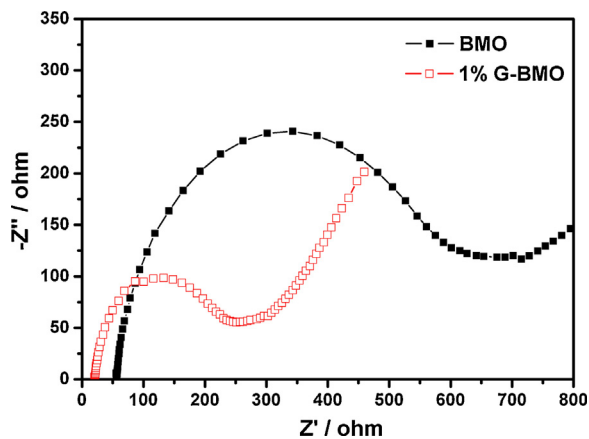


Fig. 9. Mott–Schottky plots of BMO and 1%G-BMO electrodes.

of Bi_2MoO_6 and $\text{Bi}_{3.64}\text{Mo}_{0.36}\text{O}_{6.55}$ is -0.5 and -0.34 V vs. NHE, respectively. As shown in Fig. S8, the E_g values of Bi_2MoO_6 and $\text{Bi}_{3.64}\text{Mo}_{0.36}\text{O}_{6.55}$ are 2.55 and 2.68 V, respectively. According to the empirical formula: $E_{CB} = E_{VB} - E_g$, the valence band (VB) of Bi_2MoO_6 and $\text{Bi}_{3.64}\text{Mo}_{0.36}\text{O}_{6.55}$ are 2.05 and 2.34 V, respectively. Based on the experimental results, the possible pathways for the transfer of photogenerated charge carriers are summarized and illustrated in Fig. 10. Due to the matching of energy levels, the photogenerated electrons easily transfer from the CB of Bi_2MoO_6 and $\text{Bi}_{3.64}\text{Mo}_{0.36}\text{O}_{6.55}$ to the GR layers, whereas the photogenerated holes in the VB of $\text{Bi}_{3.64}\text{Mo}_{0.36}\text{O}_{6.55}$ flow into the VB of Bi_2MoO_6 , resulting in facile separation of photogenerated charge carriers and the promotion of photodegradation efficiency.

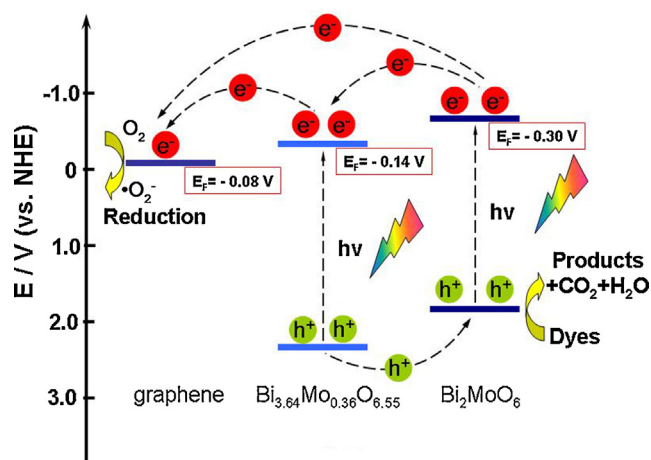


Fig. 10. Energy band diagram and photocatalytic scheme of G-BMO.

4. Conclusions

In summary, a series of heterostructured G-BMO composites with different GO additions were fabricated through a facile one-step hydrothermal method. For the first time, GO was demonstrated as a structure-directing and morphology-controlling agent. The experimental results reveal that the composition, structure and morphology of bismuth molybdate can be well controlled by regulating the GO amount without the need of using other templates. A possible mechanism for the formation of G-BMO materials is proposed. A study of the photodegradation of RhB over the G-BMO catalysts revealed that photocatalytic activities are closely related to the composition, morphology and structure of catalysts. Compared with BMO, the heterostructured G-BMO composites exhibit much better performance due to the matching band structures of BMO and GR as well as the higher carrier transmission rate of GR. A new photocatalytic mechanism is put forward to explain the effectiveness of interfacial charge transfer as well as the photocatalytic efficiency of the ternary heterostructured composites. Overall, the present work opens an avenue for the controlled synthesis of effective photocatalysts as well as directs our attention to consider the new roles of GR and GO in the controllable synthesis of new materials.

Acknowledgements

We gratefully acknowledge the financial support of the NSF of China (51238002, 51272099, 51378246, and 20801026), the NSF of Jiangxi Province (KJLD12002, 20133ACB21001, 20122BCB23013, and 20114BAB203005), and the Foundation of State Key Laboratory of Structural Chemistry (20100015).

Appendix A. Supplementary data

Supplementary material related to this article can be found, in the online version, at <http://dx.doi.org/10.1016/j.apcatb.2014.03.038>.

References

- [1] (a) C. Burda, X.B. Chen, R. Narayanan, M.A. El-Sayed, *Chem. Rev.* 105 (2005) 1025–1102; (b) Y.J. Xiong, J.M. McLellan, J. Chen, Y.D. Yin, Z.Y. Li, Y.N. Xia, *J. Am. Chem. Soc.* 127 (2005) 17118–17127.
- [2] (a) W.N. Li, J. Yuan, X.F. Shen, S. Gomez-Mower, L.P. Xu, S. Sithambaram, M. Aindow, S.L. Suib, *Adv. Funct. Mater.* 16 (2006) 1247–1253; (b) G.Z. Shen, Y. Bando, D. Golberg, *Appl. Phys. Lett.* 88 (2006) 123107–123107.
- [3] L.P. Zhu, H.M. Xiao, W.D. Zhang, Y. Yang, S.Y. Fu, *Cryst. Growth Des.* 8 (2008) 1113–1118.
- [4] S. Wang, W. Guan, D. Ma, X. Chen, L. Wan, S. Huang, J. Wang, *Cryst. Eng. Commun.* 12 (2010) 166–171.
- [5] (a) H.Y. Fan, K. Yang, D.M. Boye, T. Sigmon, K.J. Malloy, H. Xu, G.P. López, C.J. Brinker, *Science* 304 (2004) 567–571; (b) J. Hu, L. Ren, Y. Guo, H. Liang, A. Cao, L. Wan, C. Bai, *Angew. Chem., Int. Ed.* 44 (2005) 1269–1273.
- [6] S. Cho, E. Lee, H. Lee, J. Kim, Y. Kim, *Adv. Mater.* 18 (2006) 60–65.
- [7] (a) L.R. Lorzenzo, J.M.R. Herrera, J.P. Juste, R.A.A. Puebla, L.M.L. Marzán, *J. Mater. Chem.* 21 (2011) 11544–11549; (b) M. Suttipong, N.R. Tummala, B. Kitiyanan, A. Striolo, *J. Phys. Chem. C* 115 (2011) 17286–17296; (c) N.R. Tummala, A. Striolo, *ACS Nano* 3 (2009) 595–602.
- [8] (a) J.S. Chen, J. Liu, S.Z. Qiao, R. Xu, X.W. Lou, *Chem. Commun.* 47 (2011) 10443–10445; (b) H.P. Wang, J.K. Keum, A. Hiltner, E. Baer, B. Freeman, A. Rozanski, A. Galeski, *Science* 323 (2009) 757–760.
- [9] Z. Ma, J.H. Yu, S. Dai, *Adv. Mater.* 22 (2010) 261–285.
- [10] (a) L. Xu, X.Y. Yang, Z. Zhai, W.H. Hou, *Cryst. Eng. Commun.* 13 (2011) 7267–7275; (b) S. Cho, J.W. Jang, S.H. Jung, B.R. Lee, E. Oh, K.H. Lee, *Langmuir* 25 (2009) 3825–3831; (c) W.Q. Cai, J.G. Yu, B. Cheng, B.L. Su, M. Jaroniec, *J. Phys. Chem. C* 113 (2009) 14739–14746.
- [11] (a) A.K. Geim, *Science* 324 (2009) 1530–1534; (b) C. Lee, X.D. Wei, J.W. Kysar, J. Hone, *Science* 321 (2008) 385–388; (c) O. Akhavan, *ACS Nano* 4 (2010) 4174–4180.
- [12] Y.F. Lee, K.H. Chang, C.C. Hu, Y.H. Lee, *J. Mater. Chem.* 21 (2011) 14008–14012.
- [13] S. Wang, B.M. Goh, K.K. Manga, Q.L. Bao, P. Yang, K.P. Loh, *ACS Nano* 4 (2010) 6180–6186.
- [14] D.H. Wang, R. Kou, D. Choi, Z.G. Yang, Z. Nie, J. Li, L.V. Saraf, D.H. Hu, J.G. Zhang, G.L. Graff, J. Liu, M.A. Pope, I.A. Aksay, *ACS Nano* 4 (2010) 1587–1595.
- [15] S. Park, R.S. Ruoff, *Nat. Nanotechnol.* 4 (2009) 217–224.
- [16] (a) X.M. Chen, G.H. Wu, J.M. Chen, X. Chen, Z.X. Xie, X.R. Wang, *J. Am. Chem. Soc.* 133 (2011) 3693–3695; (b) N.N. Zhang, H.X. Qiu, Y. Liu, W. Wang, Y. Li, X.D. Wang, J.P. Gao, *J. Mater. Chem.* 21 (2011) 11080–11083.
- [17] (a) S. Roy, N. Soin, R. Bajpai, D.S. Misra, J.A. McLaughlin, S.S. Roy, *J. Mater. Chem.* 21 (2011) 14723–14725; (b) D. Chen, H.B. Feng, J.H. Li, in press.
- [18] C. Mattevi, G. Eda, S. Agnoli, S. Miller, K.A. Mkhoyan, O. Celik, D. Mastrogianni, G. Granozzi, E. Garfunkel, M. Chhowalla, *Adv. Funct. Mater.* 19 (2009) 2577–2583.
- [19] J. Kim, L.J. Cote, F. Kim, W. Yuan, K.R. Shull, J.X. Huang, *J. Am. Chem. Soc.* 132 (2010) 8180–8186.
- [20] (a) C.M.C. Vera, R. Aragona, *J. Solid State Chem.* 181 (2008) 1075–1079; (b) L. Zhou, W.Z. Wang, L.S. Zhang, *J. Mol. Catal. A: Chem.* 268 (2007) 195–200.
- [21] (a) H.H. Li, C.Y. Liu, K.W. Li, H. Wang, *J. Mater. Sci.* 43 (2008) 7026–7034; (b) X. Zhao, T. Xu, W. Yao, Y. Zhu, *Appl. Surf. Sci.* 255 (2009) 8036–8040.
- [22] (a) G.H. Tian, Y.J. Chen, W. Zhou, K. Pan, Y.Z. Dong, H.G. Fu, *J. Mater. Chem.* 21 (2011) 887–892; (b) L.W. Zhang, T.G. Xu, X. Zhao, Y.F. Zhu, *Appl. Catal. B: Environ.* 98 (2010) 138–146.
- [23] J.P. Zou, S.L. Luo, L.Z. Zhang, J. Ma, S.L. Lei, L.S. Long, X.B. Luo, Y. Luo, G.S. Zeng, C.T. Au, *Appl. Catal. B: Environ.* 140 (2013) 608–618.
- [24] E.P. Gao, W.Z. Wang, M. Shang, J.H. Xu, *Phys. Chem. Chem. Phys.* 13 (2011) 2887–2893.
- [25] D.C. Marcano, D.V. Kosynkin, J.M. Berlin, A. Sinitskii, Z.Z. Sun, A.S. Slesarve, L.B. Alemann, W. Lu, J.M. Tour, *ACS Nano* 4 (2010) 4806–4814.
- [26] (a) X.J. Liu, L.K. Pan, T. Lv, T. Lu, G. Zhu, Z. Sun, C.Q. Sun, *Catal. Sci. Technol.* 1 (2011) 1189–1193; (b) Y.L. Chen, Z.A. Hu, Y.Q. Chang, H.W. Wang, Z.Y. Zhang, Y.Y. Yang, H.Y. Wu, *J. Phys. Chem. C* 115 (2011) 2563–2571.
- [27] W.B. Hu, W.M. Tong, L.P. Li, J. Zheng, G.S. Li, *Phys. Chem. Chem. Phys.* 13 (2011) 11634–11643.
- [28] J. Ren, W.Z. Wang, M. Shang, S.M. Sun, E.P. Gao, *ACS Appl. Mater. Interfaces* 3 (2011) 2529–2533.
- [29] (a) G. Eda, M. Chhowalla, *Adv. Mater.* 22 (2010) 2392–2415; (b) W. Qian, R. Hao, Y.L. Hou, Y. Tian, C.M. Shen, H.J. Gao, X.L. Liang, *Nano Res.* 2 (2009) 706–712.
- [30] X. Mei, J. Ouyang, *Carbon* 49 (2011) 5389–5397.
- [31] S. Stankovich, D.A. Dikin, R.D. Piner, K.A. Kohlhaas, A. Kleinhammes, Y. Jia, Y. Wu, S.T. Nguyen, R.S. Ruoff, *Carbon* 45 (2007) 1558–1565.
- [32] (a) S. Guo, D. Wen, Y. Zhai, S. Dong, E. Wang, *ACS Nano* 4 (2010) 3959–3968; (b) T.N. Lambert, C.A. Chavez, B. Hernandez-Sanchez, P. Lu, N.S. Bell, A. Ambrosini, T. Friedman, T.J. Boyle, D.R. Wheeler, D.L. Huber, *J. Phys. Chem. C* 119 (2009) 19812–19823.
- [33] (a) F. Zhou, R. Shi, Y.F. Zhu, *J. Mol. Catal. A: Chem.* 340 (2011) 77–82; (b) M. Shang, W.Z. Wang, H.L. Xu, *Cryst. Growth Des.* 9 (2009) 991–996.
- [34] S. Stankovich, R. Piner, S. Nguyen, R. Ruoff, *Carbon* 44 (2006) 3342–3347.
- [35] (a) Y. Zhang, Z.R. Tang, X. Fu, Y.J. Xu, *ACS Nano* 5 (2011) 7426–7435; (b) K. Woan, G. Pyrgiotakis, W. Sigmund, *Adv. Mater.* 21 (2009) 2233–2239.

- [36] (a) W. Chen, S. Li, C. Chen, L. Yan, *Adv. Mater.* 23 (2011) 5679–5683;
(b) D.Z. Chen, H.Y. Quan, J.F. Liang, L. Guo, *Nanoscale* 5 (2013) 9684–9689.
- [37] Q. Liu, Z.F. Liu, X.Y. Zhang, L.Y. Yang, N. Zhang, G.L. Pan, S.G. Yin, Y.S. Chen, J. Wei, *Adv. Funct. Mater.* 19 (2009) 894–904.
- [38] L.W. Zhang, H.B. Fu, Y.F. Zhu, *Adv. Funct. Mater.* 18 (2008) 2180–2189.
- [39] M.C. Long, W.M. Cai, H. Kisch, *Chem. Phys. Lett.* 461 (2008) 102–105.
- [40] (a) X. Wang, L. Zhi, K. Mullen, *Nano Lett.* 8 (2008) 323–327;
(b) Y.B. Tang, C.S. Lee, J. Xu, Z.T. Liu, Z.H. Chen, Z. He, Y.L. Cao, G. Yuan, H. Song, L. Chen, L. Luo, H.M. Cheng, W.J. Zhang, I. Bello, S.T. Lee, *ACS Nano* 4 (2010) 3482–3488.
- [41] A. Ishikawa, T. Takata, J.N. Kondo, M. Hara, H. Kobayashi, K. Domen, *J. Am. Chem. Soc.* 124 (2002) 13547–13553.